ANNUAL REVIEWS

Annual Review of Physical Chemistry

Classical and Nonclassical Nucleation and Growth Mechanisms for Nanoparticle Formation

Young-Shin Jun,[1] Yaguang Zhu,[1] Ying Wang,[1] Deoukchen Ghim,[1] Xuanhao Wu,[2] Doyoon Kim,[1] and Haesung Jung[3]

[1]Department of Energy, Environmental and Chemical Engineering, Washington University in St. Louis, St. Louis, Missouri; email: ysjun@wustl.edu, yaguangzhu@wustl.edu, w.ying@wustl.edu, dghim@wustl.edu, doyoon@wustl.edu

[2]Department of Chemical and Environmental Engineering, Yale University, New Haven, Connecticut; email: xuanhao.wu@yale.edu

[3]School of Civil, Environmental and Chemical Engineering, Changwon National University, Changwon, South Korea; email: haesung.jung@changwon.ac.kr

Annu. Rev. Phys. Chem. 2022. 73:453–77

First published as a Review in Advance on February 3, 2022

The *Annual Review of Physical Chemistry* is online at physchem.annualreviews.org

https://doi.org/10.1146/annurev-physchem-082720-100947

Keywords

classical nucleation theory, nonclassical nucleation theory, crystal growth, oriented attachment, phase transformation, interfacial structure

Abstract

All solid materials are created via nucleation. In this evolutionary process, nuclei form in solution or at interfaces, expand by monomeric growth and oriented attachment, and undergo phase transformation. Nucleation determines the location and size of nuclei, whereas growth controls the size, shape, and aggregation of newly formed nanoparticles. These physical properties of nanoparticles can affect their functionalities, reactivities, and porosities, as well as their fate and transport. Recent advances in nanoscale analytical technologies allow in situ real-time observations, enabling us to uncover the molecular nature of nuclei and the critical controlling factors for nucleation and growth. Although a single theory cannot yet fully explain such evolving processes, we have started to better understand how both classical and

nonclassical theories can work together, and we have begun to recognize the importance of connecting these theories. This review discusses the recent convergence of knowledge about the nucleation and growth of nanoparticles.

1. INTRODUCTION

The nucleation and growth of nanoparticles play vital roles in such research fields as chemistry (1, 2), geology (3–6), biology (7, 8), physics (9), materials science (10, 11), and environmental remediation (12–14). In the natural environment, changes in the reactive surface area during mineral nucleation and growth create heterogeneities in the mineral phase and texture in sediments and soils (3). In particular, iron and manganese (hydr)oxides form ubiquitously and act as both natural electron donors and acceptors, contributing to geochemical redox cycling (4–6) and affecting the fate and transport of heavy metals and other toxic anions (14). In the atmosphere, the nucleation of sub-2-nm atmospheric aerosols and their growth can significantly affect direct/indirect radiative forcing, altering climate (1). In engineered environmental systems, the nucleation and growth of calcium carbonate, calcium sulfate, and barium sulfate cause scaling in membrane desalination systems and oil pipelines (12, 13). In biological systems, macromolecules in organisms direct nanocrystal nucleation and growth to build vertebrate skeletal systems (i.e., calcium phosphate mineral formation with collagen), mollusk shells, and other rigid biological structures (7, 8). In materials design and transformative manufacturing, controlling the nucleation and growth of nanocrystals is critical to achieving on-demand sizes, crystal structures, and shapes with unique optical, electrical, thermal, and mechanical properties (10, 11). Because of the immense importance of solid nucleation and growth, the last few decades have seen much new experimental research and diverse interpretations of its findings. Now we face the important task of connecting the advanced understanding of these systems gained from experimental results with a robust theoretical framework that integrates both classical and nonclassical nucleation and growth mechanisms.

This review presents the current experimental understanding of the nucleation and growth of nanoparticles and the theoretical approaches to describe these processes. It focuses on the nucleation and growth of solids from solution rather than on liquid condensation from the gas phase or new solid nucleation from pre-existing solids. First, the review highlights advanced experimental approaches that provide high spatiotemporal resolution, which enable observations or quantifications of the nucleation and growth of nanoparticles (Section 2). Second, we introduce classical and nonclassical nucleation and growth theories, and recent experimental findings and their relation to these theories (Sections 3–5). Because a better understanding of the elusive phenomena of solid formation can enable powerful control of the processes involved, we direct further attention to the key factors controlling the nucleation and growth of nanoparticles in complicated environments (Section 6). Finally, we present outstanding questions and future opportunities (Section 7).

2. ADVANCED EXPERIMENTAL TECHNIQUES FOR DETECTING EVOLVING NANOPARTICLES

Recent advances in real-time and nanoscale analytical techniques allow us to capture the dynamic nucleation and growth processes of nanoparticles (15). Previously, to observe these processes on long timescales (greater than minutes) (16), researchers have made changes in the aqueous chemistry (e.g., pH and precursor concentrations) (17) and observed the nanoparticle growth using optical microscopies (18) and ex situ electron microscopies (19). However, these approaches have

suffered from low resolution, low detection limits, and sample phase changes during the sample preparation or measurement. To address these limitations and to accurately reveal the fast dynamics of the nucleation and growth process of nanoparticles, the following new techniques have been utilized (**Figure 1**). Please note that this list is not meant to be definitive.

2.1. Liquid Phase/Cryogenic Transmission Electron Microscopy

Advanced transmission electron microscopy (TEM) techniques, such as liquid phase TEM (LP-TEM) and cryogenic TEM (cryo-TEM), greatly contribute to a deeper understanding of the dynamics of nanoparticles during their nucleation and growth. LP-TEM captures the evolution of nanoparticles in a liquid medium in a microfabricated cell with two Si_3N_4 windows separated by a 10–500-nm spacer (30). Cryo-TEM provides 3D structures of samples within a thin vitrified film of solution in which all the components have been frozen by plunge-freezing in a coolant (31). Using these specialized microscopies, recent studies have revealed the presence of intermediate clusters during nucleation and have captured the movement of nanosized precursors during growth. For example, with a dual inlet LP-TEM stage, two $CaCO_3$ polymorph formation pathways were found in supersaturated solution: (*a*) crystalline phase formation with the consumption of the amorphous phase (**Figure 1*a–c***) and (*b*) direct formation of crystalline phases without a precursor phase (**Figure 1*d–f***) (20). Cryo-TEM successfully revealed that poly(aspartic acid) strongly interacted with amorphous calcium carbonate (ACC) to cause its aggregation (**Figure 1*g*,*h***) (21). These advanced TEM techniques have provided a clearer picture of the multiple-step processes of solid nucleation and growth in early stages.

2.2. Fluid Cell Atomic Force Microscopy

Fluid cell atomic force microscopy (AFM) provides real-time observations of surface morphological evolution in solution. Solutions are introduced into a fluid cell by a syringe driver at a constant flow rate (**Figure 1*i***), and effluent from the fluid cell is collected by a fraction collector and analyzed (22). Fluid cell AFM can probe the dissolution of pre-existing surfaces (22), the nucleation of new nanoparticles (the particle density evolution) (32), particle growth (spiral/two-dimensional nucleation growth mode and step advance) (33), and their coupled processes (22). For example, Jun et al. examined manganese carbonate dissolution and the subsequent oriented growth of manganese oxide on the manganese carbonate substrate by in situ AFM (**Figure 1*j***) (22). In situ AFM measurements can also quantify nucleation rates (34), critical step lengths, and step formation energy (35, 36). Recently, an oriented face-specific nanocrystal probe of AFM was used to investigate the direction-specific interaction forces between nanocrystals (**Figure 1*k***) (23).

2.3. X-Ray Scattering

Offering high sensitivity and improved statistics, synchrotron-based X-ray scattering techniques have been used extensively to identify the sizes and phases of nanoparticles. The small-angle X-ray scattering (SAXS) technique enables a statistically improved quantification of nanoparticles' size and shape and their aggregation and arrangement (**Figure 1*l*,*m***) (24). In comparison, wide-angle X-ray scattering (WAXS) analyzes scattered electrons at larger angles, determining the crystallinity and phase of samples (37). In grazing incidence small/wide-angle X-ray scattering (GISAXS/GIWAXS), an X-ray beam is directed toward the sample surface at a grazing angle (α_i) that is close to, but smaller than, the critical angle (α_c) of the substrate. This operating geometry elongates the X-ray path length along the sample's surface, providing up to 1,000 times higher scattering intensity from nanoparticles formed on the substrate (**Figure 1*n*,*o***) (24, 26, 38).

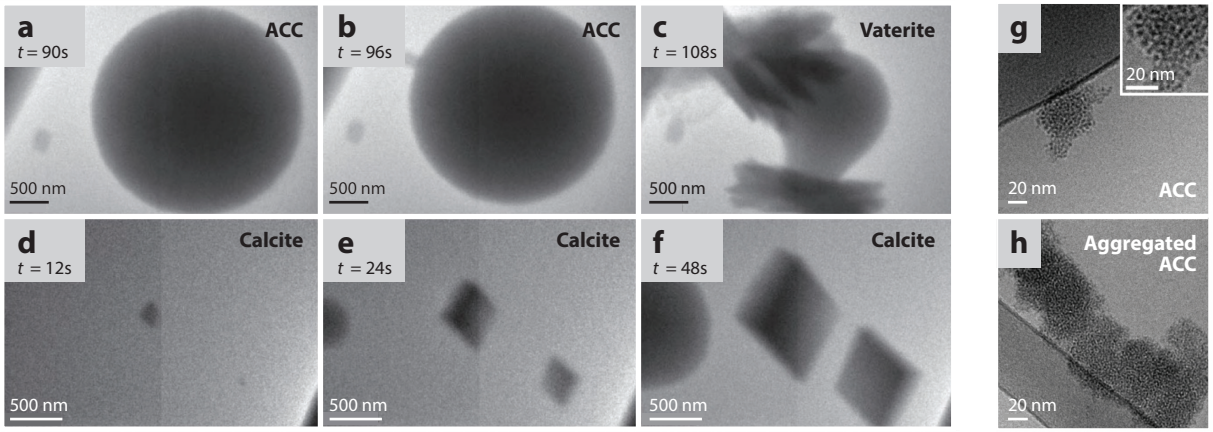

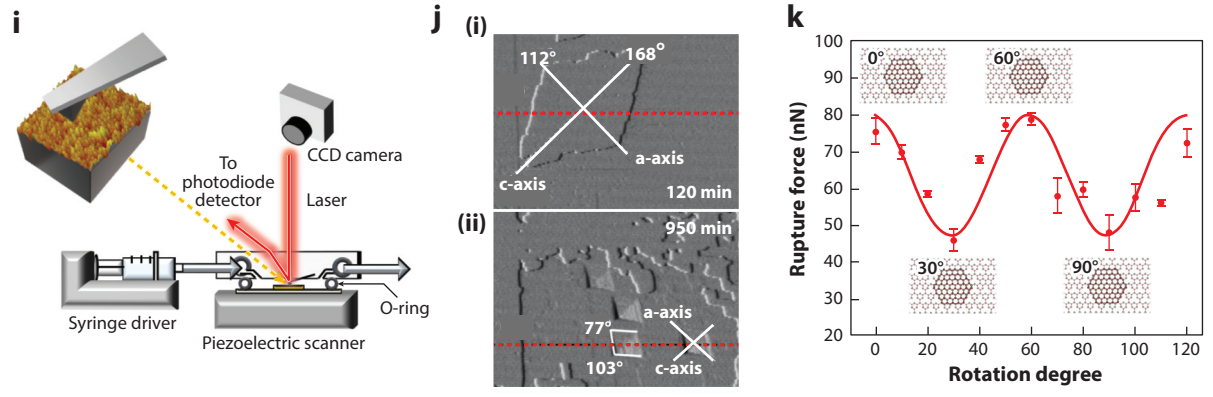

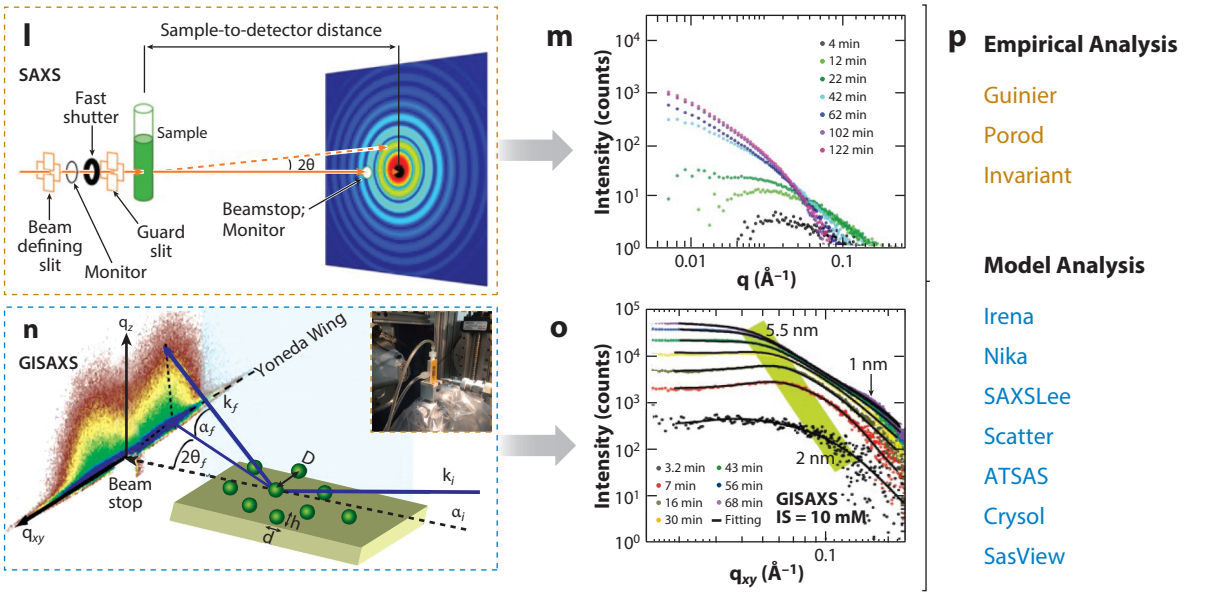

(*Caption appears on following page*)

Figure 1 (*Figure appears on preceding page*)

Advanced techniques for observing solid nucleation and growth. (*a–f*) LP-TEM observations of phase transformation from ACC to vaterite (*a–c*) and direct calcite nucleation (*d–f*). Panels *a–f* adapted with permission from Reference 20; copyright 2014 American Association for the Advancement of Science. (*g–h*) Cryo-TEM observations of aggregation of ACC caused by poly(aspartic acid). Panels *g* and *h* adapted with permission from Reference 21; copyright 2018 Springer Nature. (*i*) Schematic of fluid–cell AFM. (*j*) Subpanel *i* shows a manganese oxide island formed on manganese carbonate during a 120-min exposure to solution; subpanel *ii* shows simultaneous formation of dissolution pits of manganese carbonate and manganese oxide islands and their coalescence after 950 min. Panel adapted with permission from Reference 22; copyright 2005 American Chemical Society. (*k*) The rupture forces of the ZnO(0001)–ZnO(000$\bar{1}$) system in aqueous solution at different azimuthal orientations, after modeling fitting. Panel adapted with permission from Reference 23; copyright 2017 Springer Nature. (*l*) Schematic showing the SAXS system and the 2D scattering data obtained at beamline 12-ID-B at the APS at Argonne National Laboratory. Panel adapted with permission from Reference 24; copyright 2016 American Chemical Society. (*m*) A representative 1D SAXS image showing the relationship between the intensity, *I*, and the scattering vector, **q**, of a system with homogeneous nucleation of iron(III) (hydr)oxide nanoparticles in solution. Panel adapted with permission from Reference 25; copyright 2012 American Chemical Society. (*n*) Schematic showing the GISAXS system and the 2D scattering data. Panel adapted with permission from Reference 26; copyright 2010 American Chemical Society. (*n*, *inset*) A picture showing the in situ GISAXS experiment setup at beamline 12-ID-B at APS. Panel adapted with permission from Reference 27; copyright 2020 American Chemical Society. (*o*) A representative 1D GISAXS figure showing the heterogeneous nucleation of iron(III) (hydr)oxide nanoparticles on quartz at $[Fe^{3+}] = 10^{-4}$ M, IS = 10 mM, and pH 3.6. Nanoparticles formed with a 2-nm radius and grew to a 5.5-nm radius within 70 min; secondary 1-nm radius particles developed later. Panel adapted with permission from Reference 26; copyright 2010 American Chemical Society. (*p*) Empirical analysis approximations—the Guinier (28), the Porod (29), and the invariant approximation (24); and software packages developed for SAXS data analysis (24): Irena, Nika, SAXSLee, Scatter, ATSAS, Crysol, and SasView. Abbreviations: ACC, amorphous calcium carbonate; AFM, atomic force microscopy; APS, Advanced Photon Source; CCD, charge coupled device; cryo-TEM, cryogenic TEM; GISAXS, grazing incidence small-angle X-ray scattering; IS, ionic strength; LP-TEM, liquid phase TEM; SAXS, small-angle X-ray scattering; TEM, transmission electron microscopy.

In particular, GISAXS is highly effective in determining the size and shape of nanoparticles at interfaces (26, 39), and GIWAXS can detect the crystallinities and chemical phases of newly formed nanoparticles on surfaces (27, 40).

3. CLASSICAL AND NONCLASSICAL NUCLEATION THEORY

3.1. Classical Nucleation Theory

Classical nucleation theory (CNT) provides a good framework for explaining solid nucleation. The mathematical foundation for CNT was derived by Gibbs in the 1870s (41) and further developed by Volmer & Weber (42), Farkas (43), Becker & Döring (44), and Zeldovich (45). In CNT, a nucleus is regarded as a sphere with a surface tension equal to a theoretical flat interface (a capillarity approximation) and is assumed to be stable once formed (46). Quantitatively, the free energy of nucleation (ΔG) can be expressed as the sum of the bulk free energy and the surface free energy (Equation 1). At the critical nucleus size, the free energy of nucleation (ΔG) reaches its maximum (see **Figure 2*a***), where the free energy is called the nucleation energy barrier (ΔG^*). After overcoming ΔG^*, nuclei are stabilized and start to grow (**Figure 2*a*** and **2*b***). Hence, ΔG^* can control the nucleation rate (J), as expressed in Equation 2. Depending on whether a foreign substrate is present, nucleation can be divided into homogeneous nucleation (nucleation in solution) (47) and heterogeneous nucleation (nucleation on a substrate) (48):

$$\Delta G = -\frac{4}{3}\pi r^3\left(\frac{\Delta\mu}{v_m}\right) + 4\pi r^2\alpha, \qquad 1.$$

$$J = J_0 e^{\left(-\frac{\Delta G^*}{k_B T}\right)} = A e^{\left(-\frac{E_a}{k_B T}\right)} e^{\left(-\frac{\Delta G^*}{k_B T}\right)}, \text{ where } \Delta G^* = \frac{16\pi {v_m}^2(\alpha \text{ or } \alpha')^3}{3{k_B}^2 T^2 \sigma^2}, \qquad 2.$$

where r is the radius of the nuclei, and $\Delta\mu$ is the chemical potential [$=k_B T\sigma$; saturation, $\sigma = \ln(IAP/K_{sp})$]. IAP is the ion activity product and K_{sp} is the solubility product, v_m is the molecular

volume of the nucleated phase ($cm^3 \cdot molecule^{-1}$), α is the interfacial energy for homogeneous nucleation ($mJ \cdot m^{-2}$), α' is the effective interfacial energy for heterogeneous nucleation ($mJ \cdot m^{-2}$), J_0 is a kinetic factor related to ion diffusion and nuclei surface properties, A is a pre-exponential kinetic factor related to ion diffusion and nuclei surface properties, and E_a is the apparent activation energy ($J \cdot mol^{-1}$). k_B is the Boltzmann constant ($1.38 \times 10^{-23}\ J \cdot K^{-1}$), and T is the temperature (K).

Recently, nanoscale advanced techniques have enabled a more comprehensive understanding of nucleation, especially its thermodynamic and kinetic aspects (α, J_0, ΔG^*, and E_a). Using Equation 2, α (or α') and J_0 can be calculated, respectively, from the slope and y-intercept in a linear regression analysis of ln (J) versus $1/\sigma^2$. Utilizing the obtained α (or α'), ΔG^* can also

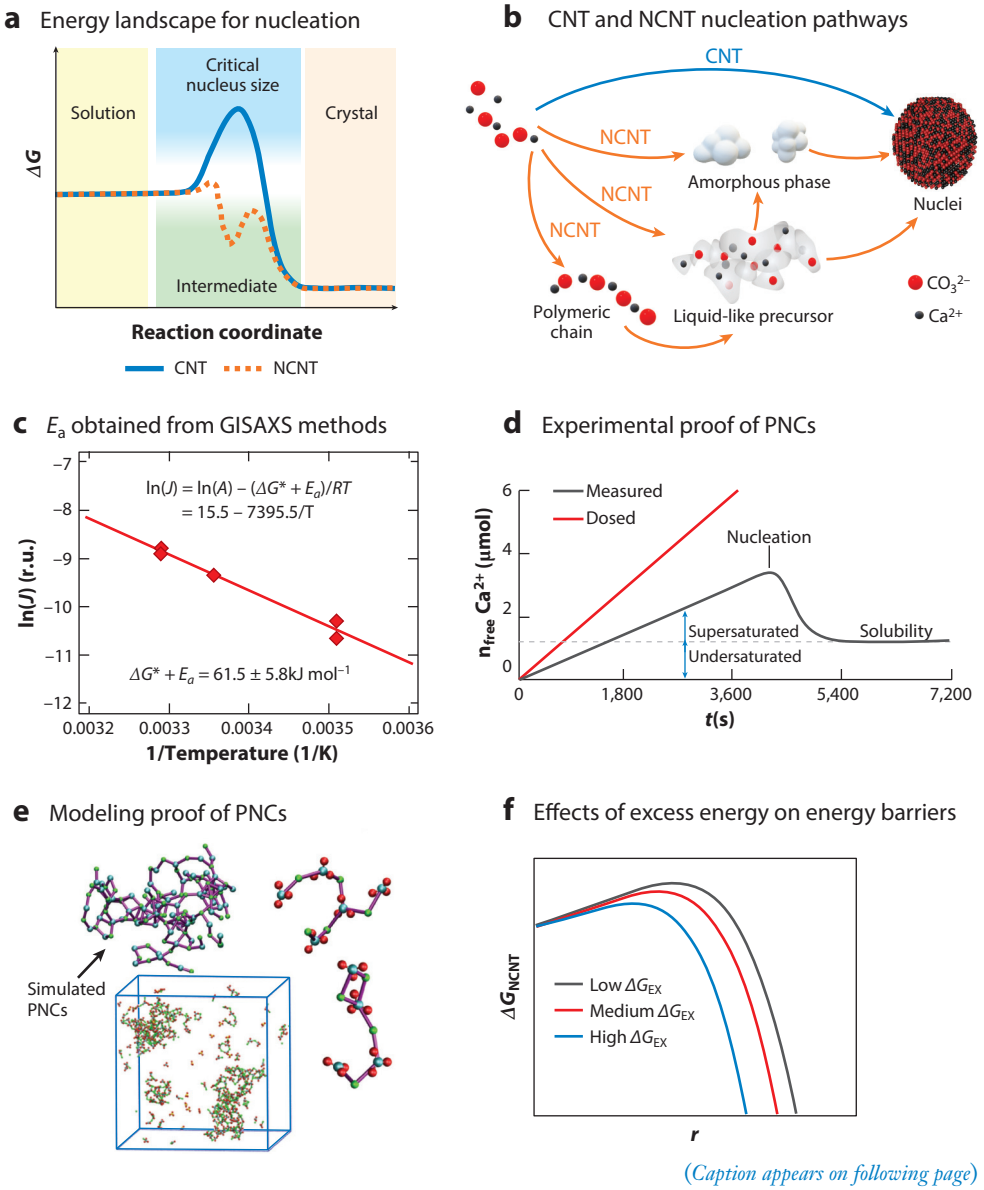

(*Caption appears on following page*)

Figure 2 (*Figure appears on preceding page*)

Nucleation theories and new experimental findings. (*a*) Energy landscapes for CNT and NCNT. (*b*) CNT and NCNT nucleation pathways. (*c*) The natural logarithm of nucleation rates [ln(*J*)] versus 1/temperature, which provides the sum of ($\Delta G^* + E_a$) from the slope. *R* is the ideal gas constant (8.314 J mol^{-1} K^{-1}). Figure adapted with permission from Reference 49; copyright 2018 Springer Nature. (*d*) Comparison of the amounts of calcium ions added (*red*) and actually detected (*black*) to determine nucleation rates. Panel adapted from Reference 50; copyright 2008 American Association for the Advancement of Science. (*e*) Molecular dynamics simulation of calcium (bi)carbonate species at high pH with a snapshot of the simulation box for 0.5 M. Panel adapted with permission from Reference 50; copyright 2008 American Association for the Advancement of Science. (*f*) Incorporation of excess free energy (ΔG_{EX}) can lower the nucleation barrier. Results obtained from Equation 3 are calculated based on Reference 51. ΔG_{EX} is related to the interfacial energy of PNCs. Low, medium, and high ΔG_{EX} plots reflect the ratios between the interfacial energy of PNCs and the interfacial energy of nuclei, within the range of 1/8 to 1/15. Abbreviations: CNT, classical nucleation theory; GISAXS, grazing incidence small-angle X-ray scattering; NCNT, nonclassical nucleation theory; PNC, prenucleation cluster.

be calculated. Here, the substrates' structure and surface properties can significantly affect α. With GISAXS, Li et al. quantified the α' values of $CaCO_3$ nucleation on mica and quartz to be 24 $mJ \cdot m^{-2}$ and 32 $mJ \cdot m^{-2}$ for vaterite–mica and vaterite–quartz systems, respectively (3). The smaller α' for vaterite–mica resulted from the smaller structural mismatch between $CaCO_3$ nuclei and mica than quartz. Hamm et al. also obtained α' for calcite nucleation on different organic matrix functionalized substrates (52). Moreover, impurities in systems can affect α' (53). Zhu et al. reported that a 0.9 mol% sulfate incorporation into $CaCO_3$ increased α' by 11.7–15.4% (40). In addition to α', the J_0 of $CaCO_3$ on quartz was measured to be $10^{16.1}$ $nuclei \cdot m^{-2} \cdot min^{-1}$ at 25°C (49). Wallace et al. reported the J_0 of silica nucleation ranges from $10^{13.5}$ to $10^{14.8}$ $nuclei \cdot m^{-2} \cdot min^{-1}$ at room temperature (54). Furthermore, by varying *T*, E_a can be determined from the slope of a linear regression of ln(*J*) versus 1/*T* (**Figure 2*c***). The E_a values for $CaCO_3$ on quartz were reported to be 45 $kJ \cdot mol^{-1}$ (49), and 32.8 $kJ \cdot mol^{-1}$ for iron(III) (hydr)oxide nucleation on quartz (27). Such an accurate determination of these thermodynamic and kinetic parameters benefits the building of a holistic framework to precisely predict and control the nucleation process in the future.

3.2. Nonclassical Nucleation Theory

The spherical assumption of CNT may not be applicable when the nuclei contain fewer than 100 molecules (55), and CNT does not provide information about aggregate structures or pathways from solution to solid crystal (56). As an alternative, nonclassical nucleation theory (NCNT) was introduced to illustrate the multiple intermediate metastable stages [e.g., prenucleation clusters (PNCs)] of nucleation that can occur preceding a thermodynamically stable phase (**Figure 2*a***) (57). Both experimental and computational efforts have been made to support NCNT. Experimentally, nanometer-sized PNCs were found by titration experiments of dilute calcium chloride solution, which observed a concentration difference between the measured calcium ions' concentration and the dosed calcium ions' concentration (**Figure 2*d***) (50). The presence of PNCs with an ~2-nm diameter was further verified by analytical ultracentrifugation (AUC) of solutions drawn at different times in the prenucleation stage (50). Cryo-TEM also revealed the average diameters of PNCs to be 0.6–1.1 nm, which is smaller than that detected by AUC (58). Furthermore, electrospray ionization mass spectrometry (ESI-MS) has been utilized along with the X-ray absorption near edge structure (XANES) to show that highly hydrated networks are the PNCs for metal carbonates MCO_3 (M = Ca, Sr, Ba, Mn, Cd, and Pb) (59).

Modeling approaches such as molecular dynamics (MD) simulations have also been utilized to examine the existence of PNCs. Using MD, Demichelis et al. proposed that PNCs are composed

of dynamically ordered liquid-like oxyanion polymers (DOLLOP), including chains, branches, and rings (**Figure 2*e***) (60), yet the stability of DOLLOPs has been questioned, because they can dissociate back into free ions and ion pairs (57). Using MD, Wallace et al. suggested that clusters are droplets of a dense liquid phase of $CaCO_3 \cdot nH_2O$ that have formed by liquid–liquid separation (61). For calcium phosphate, based on ab initio MD simulations, it was found that calcium triphosphate PNC is more thermodynamically stable than free ions (62). Yang et al. demonstrated that ion association occurs between ions with the same charge and leads to calcium phosphate PNC formation via the consecutive coordination of the phosphate ions to calcium (63). Owing to the critical roles of the PNCs in understanding and controlling solid nucleation and their phase and shape evolution, examining prenucleation stages of solid formation is currently an active research area.

3.3. Relationship Between Classical and Nonclassical Nucleation

As discussed above, CNT offers a quantitative description of nucleation but does not describe the presence of intermediate stages. However, NCNT describes multiple stages and the presence of amorphous/dense liquid/metastable phases but does not provide a quantitative description of the nucleation. To more accurately describe nucleation, it is important to connect the two theories. For example, Habraken et al. found amorphous calcium phosphate (ACP) formation, but the ACP formation could not be directly reconciled with CNT. Hence, to connect CNT and NCNT, they introduced an "excess free energy (ΔG_{EX})" term, describing the impact of the PNCs on the free energy of calcium phosphate formation, as shown in Equation 3 (51):

$$\Delta G_{NCNT} = -\frac{4\pi f r^3}{3 v_m} k_B T \sigma' + 4\pi f r^2 \alpha(r) - N \Delta G_{EX}, \quad 3.$$

where ΔG_{NCNT} is the free energy of nucleation when calcium phosphate PNCs are considered; f is a geometric factor that depends on the nucleus shape, taking values of 1 and 1/2 for spherical and hemispherical nuclei, respectively; σ' is supersaturation when considering PNCs, which equals $ln(IAP/K_{sp})^{1/v}$, where v is the number of growth units in the material; $\alpha(r)$ is the interfacial energy of the nuclei; and N is the number of PNCs that combine to form the particle. ΔG_{EX}, which expresses the interfacial energy of PNCs, decreases when clusters aggregate, resulting in a lower energy barrier of calcium phosphate nucleation (**Figure 2*f***). Including ΔG_{EX} in the energy consideration helps to explain how ACP nucleates first instead of the most thermodynamically stable phase, hydroxyapatite. Similarly, the decrease in the energy barrier of calcite nucleation on carboxyl-terminated self-assembled monolayers has been estimated (64). Unfortunately, however, no experimental or modeling work has directly determined a value of ΔG_{EX}, which calls for future systematic examination.

4. CLASSICAL AND NONCLASSICAL GROWTH THEORIES

4.1. Classical Crystal Growth Theory

Using the terrace–ledge–kink model, Burton et al. formulated classical crystal growth theory, describing an atomic process in which monomeric growth units attach to pre-existing mineral surfaces (e.g., steps and kinks) and develop faceted crystals (65). For solid crystal growth from solutions, aqueous species—including ions, molecules, and atoms—are the primary constituents that incorporate into the crystal lattice (66). The overall growth rate (R) is related to σ as shown by Equation 4 (66):

$$R = k_g(\sigma - 1)^g, \quad 4.$$

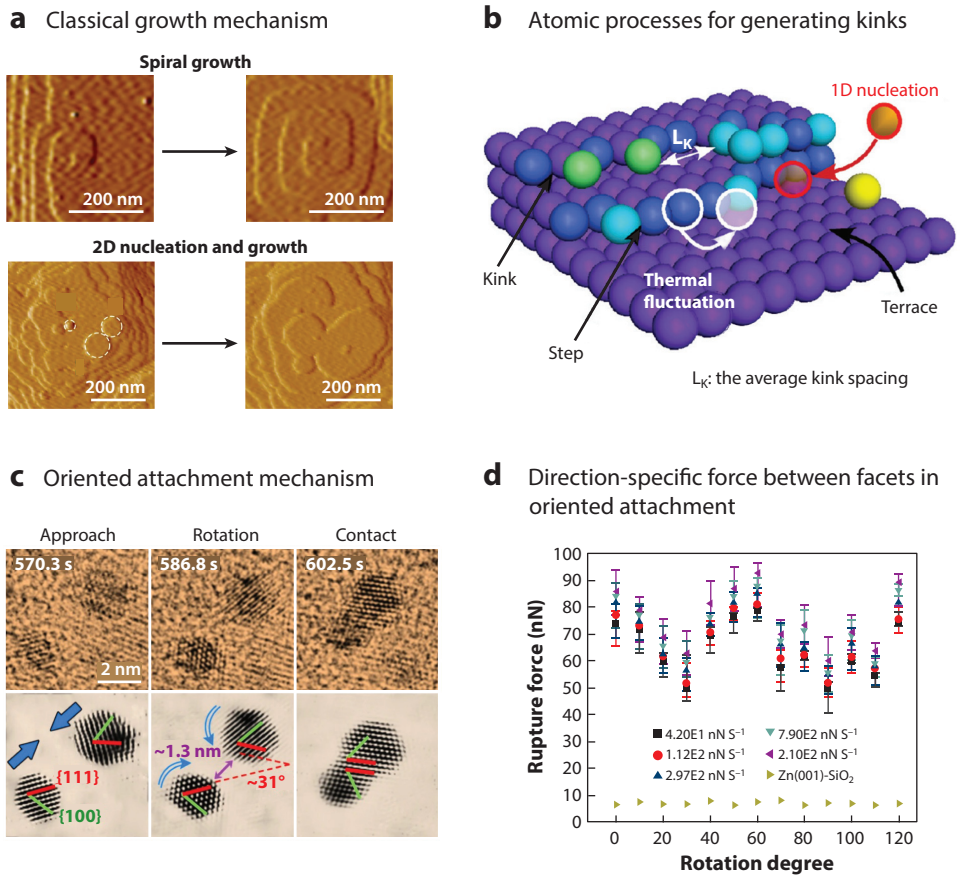

Figure 3

Growth theories and new experimental findings. (*a*) Classical growth mechanisms: spiral growth and 2D island nucleation and growth. Panel adapted with permission from Reference 67; copyright 2020 National Academy of Sciences. (*b*) Schematic illustrating terrace, steps, and kinks on a crystal surface. Kinks are created via either movements of molecules on the step edge (thermal fluctuations) or attachment of new solute molecules from solution (1D nucleation). Panel adapted with permission from Reference 68; copyright 2009 American Chemical Society. (*c*) Nonclassical growth via oriented attachment: In situ TEM measurements revealed the oriented attachment process of gold nanoparticles, including approach, rotation, and contact. Panel adapted with permission from Reference 69; copyright 2018 Springer Nature. (*d*) Direction-specific interaction forces at different azimuthal orientations for ZnO(0001)-ZnO(000$\bar{1}$) facet interactions. Different symbols represent different loading rates. Rupture force is the jump-from-contact force when the single crystal on the tip is approaching/retracting single crystal substrate. Rotation angle is the azimuthal angle between the single crystal on the tip and single crystal substrate. Panel adapted with permission from Reference 23; copyright 2017 Springer Nature. Abbreviation: TEM, transmission electron microscopy.

where k_g is the growth rate constant, which is dependent on the solubility of the materials and temperature, and g is the growth order, signifying the growth mechanism. At relatively low σ, spiral growth (**Figure 3*a***, *top*) dominates the system, and the value of g is 2, resulting in a parabolic growth law (66). When σ is increased, two-dimensional (2D) nucleation dominates the system (**Figure 3*a***, *bottom*). The growth rate changes exponentially and g takes on values larger than 2 (66). Finally, as σ increases further, the surface becomes rough, growth is dominated by mass transfer, and g is equal to 1 (66).

Although the classical growth model has been successfully applied to understanding crystallization processes for many systems (70), it has also continuously evolved. Notably, with the advent of advanced techniques, more factors (e.g., kink densities, kink site specificities, and ion pairs) have been added to classical growth theory to more precisely predict crystal growth. In the classical theory, kinks are critical for incorporating new atoms into the surface, because incoming atoms at kinks can immediately bond with more neighboring atoms than atoms on terraces and flat steps can (66). Therefore, the growth rate of a crystal, which is equivalent to the rate of molecule attachment to a pre-existing crystal, is closely related to the kink density of the surface at a fixed solute concentration. Although a high kink density is assumed in the classical view (32), Zhang & Nancollas point out that, for sparingly soluble crystals at low temperatures, the equilibrium kink density should be low, and thus kink formation is an important contributor to controlling the kinetics of step-growth (71). Under this circumstance, kinks can be generated by one-dimensional (1D) nucleation. Previously, a kinetic Monte Carlo simulation was used to describe this process (68). A solute molecule attaches to a fully occupied region of the step and creates a 1D nucleation, providing two new kink sites where further growth proceeds (**Figure 3*b***). Based on this principle, Joswiak et al. derived a supersaturation-dependent kink density expression (53).

Although the rates of attachment and detachment of precursors to kink sites are critical in determining the step advancement rate in growth, site specificities are often ignored. Stack & Grantham found that calcium-to-carbonate ratios can significantly change the growth patterns of calcite and that the attachment and detachment of aqueous calcium and carbonate ions should be treated separately (72). Therefore, for a crystal whose chemical formula is AB, we should separately consider the probability of ions A interacting with kinks and the probability of ions B interacting with kinks. Furthermore, recognizing the important roles of ion pairs as metastable phases in NCNT, recent studies have incorporated the role of ion pairs in the crystal growth (73), as shown in Equation 5:

$$R = 0.32 \cdot \frac{K_{AB,n}[A]^n[B]^n}{(1 + K_A[A])^n(1 + K_A[B])^n} \frac{k_B T}{h} e^{-\frac{\Delta G_{IP}}{RT}}. \quad 5.$$

Here, n represents the number of ion pairs in the attaching unit, $K_{AB,n}$ is the equilibrium constant for $[AB]_n$ complex formation in solution, h is Planck's constant, and ΔG_{IP} represents a reaction barrier for the formation of ion pairs.

4.2. Nonclassical Crystal Growth via Oriented Attachment

Crystal growth can occur via the organized aggregation of nanosized crystals to form micron-sized crystals, which is called oriented attachment (OA) (74, 75). As shown in **Figure 3*c***, OA has three steps: (*a*) self-assembly of primary nanocrystals (approach), (*b*) crystallographic reorganization within the self-assemblies (rotation), and (*c*) conversion to oriented aggregates (contact) (70). By harnessing OA to control the facet selectivity of materials, material scientists can design crystalline structures with very specific geometries in one, two, or three dimensions, and even create dislocations in the resulting crystal by promoting nonperfect attachment (74, 75). In this way, an improved understanding of the OA mechanism can shed light on the formation of anisotropic nanostructures and the evolution of their structural defects.

To decipher the OA process, colloidal aggregative behavior has been studied. To simulate the monodispersity of final particle sizes, early attempts at kinetic modeling had to assume that aggregation took place only between nuclei and large particles (76, 77). Eventually, this assumption was contradicted in later observations of single–single particle aggregation in LP-TEM measurements (69). To resolve this question, Huang and colleagues studied the growth of ZnS nanocrystals in the presence of mercaptoethanol and developed a model based on nanoparticle collisions (78). The

evolution of the mean diameter (d) was described in Equation 6, where d_0 is the mean diameter at $t = 0$, and k_1 is the rate constant for oriented particle attachment:

$$d = \frac{d_0\left(\sqrt[3]{2}k_1 t + 1\right)}{k_1 t + 1}. \quad 6.$$

Then, Zhang et al. further developed a multistep kinetic model based on the Smoluchowski equation, simulating the OA process with nanoparticles of varying sizes (79). To quantitatively describe the OA growth of zeolite, Tsapatsis and coworkers used the coalescence rate constant calculated from the Derjaguin–Landau–Verwey–Overbeek (DLVO) theory (80). A more recent work by Woehl & Prozorov found that the mobility of gold nanoparticles can determine whether OA happens through monomer–chain attachments or chain–chain attachments (81). The second-order aggregation kinetics revealed that the self-assembly rate increased approximately linearly with the nanoparticle diffusion coefficient.

4.2.1. Energy associated with oriented attachment. A longstanding question regarding the OA process is, What driving forces enable particles to achieve crystallographic coalignment and promote attachment-based growth? With new experimental methods, significant progress has been achieved in identifying the strength and range of the driving forces, including macroscopic interparticle interactions and interfacial water-induced interactions. Within the former, face-specific van der Waals forces (vdW) were found to insignificantly affect azimuthal alignment at particle distances of 1.0–1.5 nm, but they are critical when particle distances are only one hydration layer thick (82). Nevertheless, another study investigating mica–mica adhesion showed that electrostatic interactions are the driving force for OA at short ranges and that vdW dominates at larger particle separations (83). Interfacial water structuring also contributed to the OA process. For example, dynamic force spectroscopy using nanoengineered single-crystal probes showed that an attractive force between ZnO (0001) and ZnO($000\bar{1}$) surfaces with 60° rotational periodicity and OA was water-mediated (**Figure 3*d***) (23). Furthermore, macroscopic interparticle interactions and interfacial water-induced interactions can collaboratively control the OA process. Liu et al. illustrated that OA is driven by forces and torques arising from a combination of electrostatic ion-solvent correlations and dipolar interactions, even before the particles are within 5 nm (84).

5. SOLID SOLUTION AND PHASE TRANSFORMATION

Nucleation and growth are determined by two controlling energy factors (85): the free energy barrier (thermodynamics) and thermal energy (kinetics). These processes minimize the surface free energy in local space, making kinetically but less thermodynamically favored metastable phases form first, followed by their phase transformation to more thermodynamically favored structures. For example, ACC and ACP often appear first during nucleation (86, 87), and then they transform to more crystalline phases.

In addition to thermodynamic and kinetic energy factors, differences in the bonding geometry of amorphous particles influence the pathway of phase transformation. For instance, ACP formed at a low Ca:P ratio mainly has monodentate bonding and directly transforms to hydroxyapatite. In contrast, ACP formed at a high Ca:P ratio mainly has bidentate bonding and transforms first to brushite and then to the most thermodynamically stable form, hydroxyapatite (87). These findings indicate that the ratios of building units alter the bonding structures in amorphous particles and subsequently affect the pathways of phase transformation.

A solid solution is a mixture at the atomic level of at least two different solids that coexist as a new solid. Minor components are uniformly distributed in the crystal lattice of the major crystal

structure. Some of the most studied solid solutions are calcium–magnesium–carbonate systems. At low Mg^{2+} activity (e.g., 1.59×10^{-4}), Mg^{2+} incorporates into the calcite lattice and enhances the solubility of Mg-bearing calcite, decreasing the effective supersaturation needed for the calcites' growth (88). In another work, the metastability of ACC and amorphous magnesium carbonate (AMC) was altered by changing the Mg:(Ca+Mg) ratio (89). Furthermore, ACC's structure and its transformation pathway are also largely influenced by the addition of Mg. A recent study reported a new hydrated crystalline structure of $CaCO_3$ in the presence of Mg^{2+} (90): At an Mg:Ca molar ratio of 4.3–6.1, $CaCO_3$ hemihydrates with a needle-like crystal structure, which had not been observed previously. Here, Mg^{2+} ions in the solution slowed the crystallization of the hydrated crystalline phase of $CaCO_3$ to monohydrated calcite. These findings proved the importance of Mg incorporation into $CaCO_3$ particles in determining the growth of $CaCO_3$, its phase transformation, and its structure.

6. FACTORS AFFECTING NANOPARTICLE NUCLEATION AND GROWTH

6.1. Defects and Facets

Substrate defects, such as steps and point defects, change the binding and adsorption energy between the precursor species and the substrate, altering the nucleation and growth of nanoparticles. Using LP-TEM, Zhu et al. explored the selective oxidation of Ag nanocrystals at different planar defects, such as nanotwins and stacking faults (**Figure 4*a***) (91). Ag_2O embryos preferentially nucleated at twinned tips and stacking faults, and they grew inward along the planar defects. However, the oxidation of metal was not observed away from the twinned tip of the facet (92), suggesting that Ag_2O selectively nucleated and grew at defects.

In particular, the surface energy at facets determines the growth rate of nanoparticles, and the nanoparticles grow to minimize their own surface energy. A low-energy facet exhibits a relatively slow growth rate, whereas a high-energy facet has a fast growth rate, enabling it to have a lower nanoparticle surface energy. As representative examples, nanoparticles' shapes were controlled by modifying the surface energy of the facet with surfactant adsorption, adjusting the facet's growth rate (98, 99). However, facet growth rates are determined by their surface energy only if nanoparticles are bigger than the critical size of nanoparticles. In a study of the dynamic growth of Pt nanocubes (93), when the nanoparticles were smaller than their critical particle size (~5 nm) for facet growth (up to 70 s in **Figure 4*b***), ligands on the facets were easily removed, providing space for Pt growth. This process causes similar growth rates regardless of the facets' surface energy. After 70 s, when Pt nanoparticles grew bigger than their critical size, the growth rates of Pt nanoparticles at {111} facets were the highest, followed by those at {001} and {100} facets, indicating facet-dependent growth.

6.2. Heterogeneity of Surfaces

In nature and in engineered systems, the mineralogy and morphologies of substrate surfaces are heterogeneous, governed by their formation process and surrounding chemistry (100). Heterogeneous nucleation and growth are strongly connected with interfacial free energy and, thus, accounting for the surface heterogeneity is crucial to understanding these processes.

Heterogeneous nucleation and growth are largely influenced by the following substrate properties: its surface charge, interfacial energy, and surface morphology, and the lattice similarity between the precipitate and substrate (3, 94, 101). Hu et al. examined the heterogeneous nucleation and growth of iron(III) hydroxide on naturally abundant mineral substrates: quartz, muscovite, and corundum (**Figure 4*c***) (94). They found that the heterogeneous nucleation rate of iron(III)

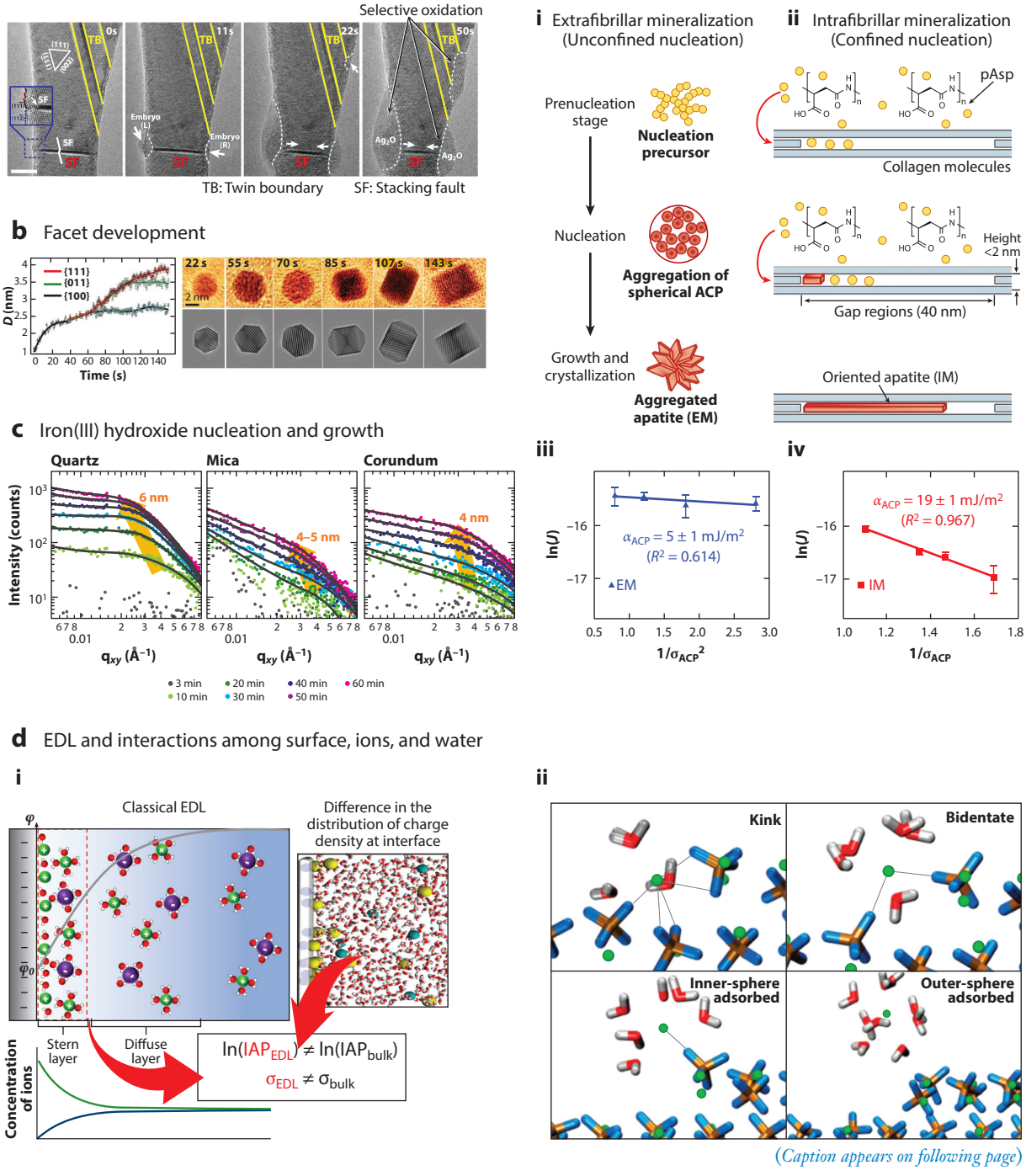

(Caption appears on following page)

Figure 4 (*Figure appears on preceding page*)

Factors affecting nanoparticle nucleation and growth. (*a*) Selective Ag_2O nucleation at different defects of Ag nanocrystals. Panel adapted with permission from Reference 91; copyright 2021 Springer Nature. (*b*) Measured distances, *D*, from the center of Pt nanoparticles to each facet, directly related to their growth rate, and sequential images of a Pt nanocube's growth. Panel adapted with permission from Reference 93; copyright 2014 American Association for the Advancement of Science. (*c*) Iron(III) (hydr)oxide heterogeneous nucleation on different substrates: quartz, mica, and corundum. Panel adapted with permission from Reference 94; copyright 2013 American Chemical Society. (*d*) Subpanel *i* shows the formation of an EDL and inhomogeneous charge distribution at the EDL. In the figure of MD simulation results, yellow and cyan spheres indicate cations and anions, respectively. MD simulation results were adapted with permission from Reference 95; copyright 2014 American Chemical Society. Subpanel *ii* shows interactions among surface, ions, and water are all important in controlling barite growth kinetics (96): bonding at kink sites, bidentate complexation, inner-sphere complexation, and outer-sphere complexation. Barium atoms are green, sulfate ions are ochre (sulfur) and blue (oxygen), oxygens atoms of water are red, and hydrogens are gray. Subpanel adapted with permission from Reference 96; copyright 2012 American Chemical Society. (*e*) Schematics of two different nucleation models for collagen mineralization. Subpanel *i* shows extrafibrillar nucleation in unconfined space, and subpanel *ii* shows intrafibrillar nucleation in a confined gap region. Subpanels *iii* and *iv* show interfacial energies for ACP nucleation (α_{ACP}) during EM and IM, calculated from the relationship between *J* and supersaturation [EM: ln(*J*) versus $1/\sigma^2$ without nanoconfinement; IM: ln(*J*) versus $1/\sigma$ with nanoconfinement] (97). Panel adapted with permission from Reference 97; copyright 2018 Springer Nature. Abbreviations: ACP, amorphous calcium phosphate; EDL, electric double layer; EM, extrafibrillar mineralization; IAP, ion activity product; IM, intrafibrillar mineralization; MD, molecular dynamics; pAsp, poly(aspartic acid).

(hydr)oxide minerals was faster on corundum than on other substrates. This fast nucleation was explained by a higher liquid–substrate interfacial energy (α_{ls}), confirmed by the water contact angle, and a lower substrate–nucleation interfacial energy (α_{sn}) from lattice similarity. In contrast, the heterogeneous growth of iron(III) (hydr)oxide on corundum was rather slower than on quartz and mica because the positively charged iron(III) (hydr)oxide embryos were electrostatically repelled from the positively charged corundum, hindering their heterogeneous growth.

Both the surface morphology and the exposed substrate facets and/or planes deserve consideration in nucleation and growth. Unlike the effects of nanoparticle facets on their growth discussed in Section 6.1, here, we discuss how the existing substrate facets and/or planes influence the heterogeneous nucleation and growth of nanoparticles. Recently, Liu et al. demonstrated how manganese oxides were facet-selectively nucleated and grown on nanohematite (102). The selective nucleation of manganese oxides occurred owing to the surface oxygen coordination and bulk electron transfer mechanism. Then manganese oxides grew along the specific direction that minimized lattice mismatch, consequently forming manganese oxide nanowires on nanohematite. Even on the same mineral substrate, the shape and structure of heterogeneously formed manganese oxides were governed by the facet of the substrate, highlighting the importance of substrate facets on the nucleation and the growth of manganese oxides.

6.3. Electronic Structure

The ubiquitous interactions between water and surfaces are centrally important in many disciplines, such as electrochemistry, materials science, and geology, (103–107). Because of the surface charge created by breaking hydrogen bonds at a surface, water molecules behave differently near the interface. Particularly, the surface charge at a solid–water interface induces an electrostatic field and consequently influences the alignment of cations, anions, and water molecules, creating an electric double layer (EDL). Because the EDL can alter reaction conditions kinetically and thermodynamically, the structure of the EDL is fundamental in the study of nanoparticle nucleation and growth. Recent studies have discussed inhomogeneous structures in the EDL resulting from ion–ion correlations (**Figure 4*d***) (95, 108). Interfacial surface charges occur as either homogeneously distributed charge densities or localized charge densities at discrete sites, depending on the identity of the cations (95, 105). The type of charge distribution affects the net orientation of

water and the pH of a solution at the interface (103, 106, 108, 109). As an example, using in situ high-resolution X-ray reflectivity, Lee et al. confirmed that the substantial enhancement of inner sphere complexed Rb^+ near negatively charged mica far exceeds the amount needed for charge compensation of the mica surface (charge overscreening) (110). Hence, a full recognition of the effect of inhomogeneous structures in the EDL is crucial to understanding how materials form owing to differences in the concentrations of ions (95, 103, 108) and pH (108, 109), subsequently altering the saturation of the solution at the solid–water interface (32). In addition, the perturbation of local water structure by ions may also facilitate transport and decrease the energy barrier to the attachment of ions to the interfaces (96). In turn, newly formed particles can generate different surface potentials and add surface heterogeneities for subsequent reactions (111).

6.4. Water and Ions at Interfaces

Multiple interactions among the solvent, the foreign substrate, and ions can mediate the nucleation and growth of solids. In solid nucleation, the transformation from ionic clusters to a dense liquid phase is closely related to liquid–liquid separation (61). Furthermore, the stability and dynamic behaviors of PNCs are strongly influenced by the water molecules (59). For example, aggregation of the PNCs was accompanied by a reduction of the mobility of water (60). In CNT, ion desolvation can determine E_a and J. In solid growth, the approach of an ion to the surface requires desolvation of both the surface and the ion, leading to a rate-limiting process for such 2D nucleation (32). A metadynamic simulation demonstrated that the rate-limiting reaction for attachment in barite growth is a conversion of the inner-sphere adsorbed species to the bidentate species (**Figure 4*d***) (96). The desolvation effect is also a primary contributor to isotopic fractionation during $CaCO_3$ precipitation (112). In the case of ion–ion interactions, stable ion pairs at the nucleation stage have been considered as PNCs (50). At the growth stage, ion pairs can also serve as precursors for growth (73).

6.5. Biological and Organic Contributions

Mineral nucleation and growth induced by microorganisms are important in understanding geological elemental cycling and the rules that govern life. There are two fundamental mechanisms for bacterially induced mineral nucleation: First, passive nucleation occurs when the solution chemistry around bacteria cells is changed by microbial activities, such as bacterial ammonification, sulfate reduction in anoxic environments, and alkalization by cyanobacteria (113). These microbial activities release CO_3^{2-} or HCO_3^- or increase the solution pH, driving minerals to nucleate and grow. Second, active nucleation happens when bacteria cell surfaces contribute as nucleation sites (114). Owing to their small size (~2 μm^3), large surface-to-volume ratio, and negative surface charge, bacteria are highly efficient at adsorbing metal cations from surrounding environments and concentrating them on their surfaces. Nucleation starts when these adsorbed cations interact with anions from the external milieu, driving the nucleation of (oxy)(hydr)oxides (115), carbonates (116), sulfates (117), sulfides (118), and phosphates (119).

In addition, soluble organic molecules or dissolved organic matter (DOM) contains high numbers of metal-binding sites, including carboxylates, phenols, amines, and thiols. Similar to microorganisms, the metal-ligand complexation of DOM alters the interactions between metal ions and aqueous anion counterparts. DOM has been shown to affect the nucleation of calcium carbonates (120), iron oxyhydroxides (121), calcium sulfate (122), metal sulfides (123), and calcium phosphate (124). DOM affects the nucleation and growth of minerals through two mechanisms. First, DOM complexes with dissolved metal ions, decreasing the mineral saturation

and the driving force for nucleation and growth (125, 126). Second, DOM adsorbs onto the surface of newly formed nanoclusters, further blocking the active growth sites for incoming new phases from the solution (121). Some organic polymers [e.g., poly(sodium 4-styrene sulfate)] can also affect the nucleation of minerals via binding with precursors (93).

6.6. Nanoconfinement

The nucleation and growth of particles in nanoscale porous media are critical in geological processes (127), biological processes (128), and engineering applications, such as the production of biopharmaceuticals (129) and semiconductors (130), and water treatment (131). In confined nanopore spaces, the physicochemical properties of particles (e.g., thermotropism or polymorphism) are distinct from those in unconfined spaces (132, 133). The structure, dynamics, and thermodynamics of water in nanoconfinement can also affect the solvation free energies of ions and clusters (134, 135), altering nucleation and growth in nanopores. For a confined space, the Gibbs–Thomson equation describes the melting point depression (ΔT_m) of materials relative to the bulk form ($T_{m,bulk}$) (132). Recently, Jin & Coasne reported a simulation study providing a molecular-level understanding of how nanoscale confinement shifts the melting point to a lower temperature (i.e., a decreased metastability barrier upon methane hydrate formation), which was previously observed experimentally and interpreted by the Gibbs–Thomson equation (136). By contrast, for particles strongly adhered to the wall ($\theta < 90^o$), the melting point may increase in the confined space.

Nanoconfinement has been considered an essential aspect of biomineralization. For example, Cantaert et al. showed that 25–300-nm pores induced the formation of polycrystalline hydroxyapatite rod crystals via an intermediate ACP phase (137). Kim et al. suggested that modification of CNT is required to understand intrafibrillar collagen mineralization (i.e., mineralization inside collagen gap regions) (97). Owing to the nanoconfinement in the gap region (40 nm long and ~2 nm high) (138), calcium phosphate mineral is forced to nucleate and grow only in a lateral dimension (**Figure 4*e***, subpanels *i* and *ii*). The 2D growth changes the relationship between nucleation rates (J) and supersaturation (σ) from $\ln(J) \propto 1/\sigma^2$ (for homogeneous nucleation of a sphere) to $\ln(J) \propto 1/\sigma$, explaining how confinement reduces the energy barrier to nucleation (**Figure 4*e***, subpanels *iii* and *iv*). In bone mineralization, the extent of calcium phosphate formation inside the collagen gap region is closely related to mechanical properties such as the elastic modulus of tissue-level collagen matrices (139). Future research can harness the improved understanding of nucleation and growth in nanoconfinement for designing and developing stronger materials.

7. OUTSTANDING QUESTIONS AND FUTURE OPPORTUNITIES

In recent decades, theoretical and experimental studies have elaborated the formation processes of nanoparticles, providing critical molecular insights into their behaviors and presenting new capabilities for controlling them (**Figure 5**). However, there are still outstanding questions that we need to address. In this section, thus, we discuss these outstanding questions and future opportunities for research and engineering in solid nucleation and growth.

7.1. Developing a Holistic Model to Quantitatively Describe Nucleation and Growth

A holistic quantitative description of nucleation and growth remains a great challenge. Here, we share our perspectives on building a more complete quantitative model, one which unites classical and nonclassical nucleation and growth behaviors. In the nonclassical nucleation process, PNCs,

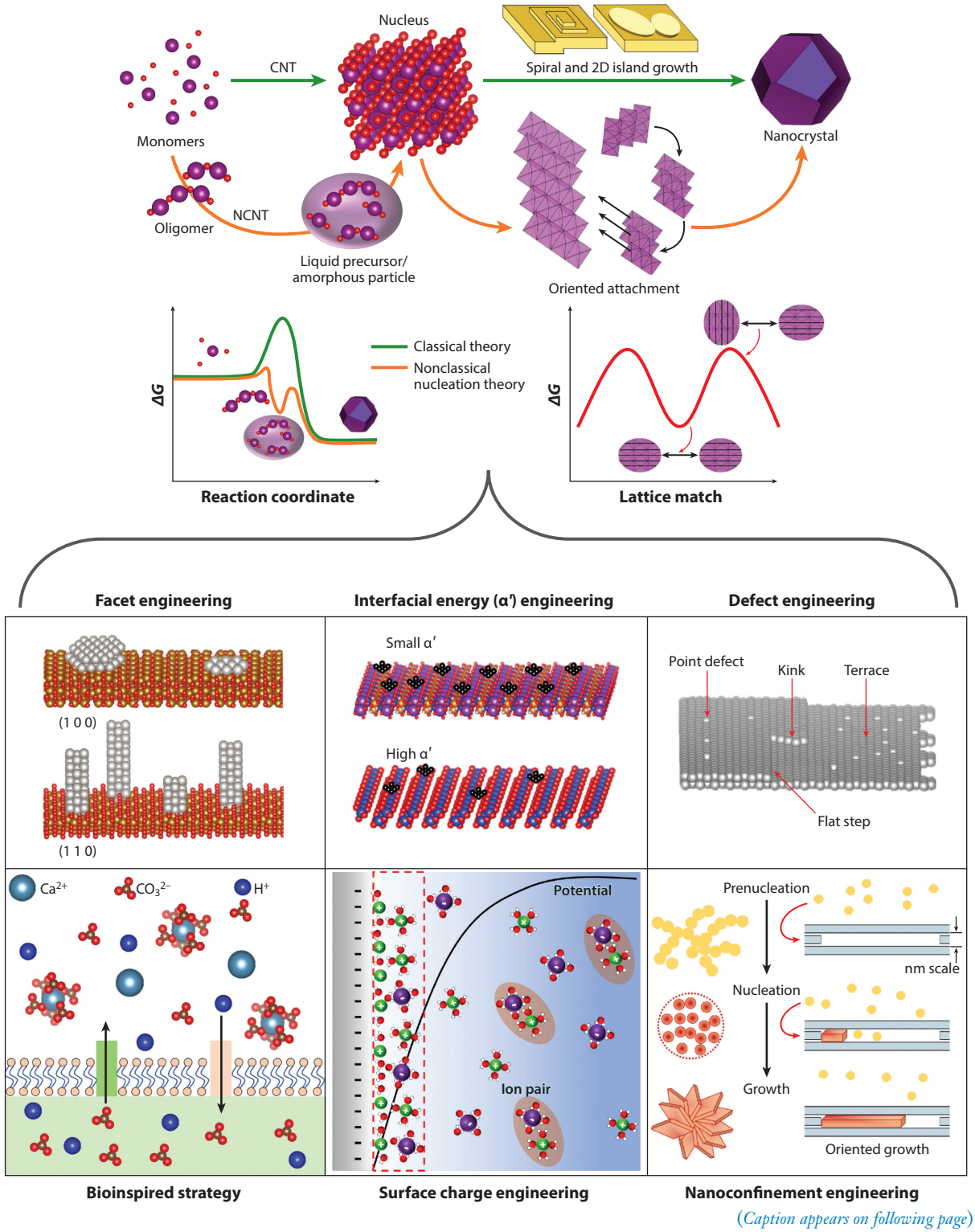

(Caption appears on following page)

Figure 5 (*Figure appears on preceding page*)

Perspectives toward a holistic understanding of classical and nonclassical nucleation and growth mechanisms, and determining factors in engineering nanoparticles and understanding their behavior. Theoretical and experimental approaches can yield a comprehensive model connecting the nucleation and the growth behaviors of nanoparticles. Such model development can predict the behavior and formation of nanoparticles more accurately, enabling us to design and predict their properties in engineering fields and nature. The middle row left ΔG figure illustrates the free energy landscapes in classical and nonclassical nucleation and classical growth pathways. Here, classical theory includes both nucleation and growth. The middle right ΔG figure portrays the free energy landscape during a nonclassical growth pathway via oriented attachment. Panels for surface charge engineering and nanoconfinement engineering were adapted with permission from References 95 and 97, respectively; copyright 2014 American Chemical Society and copyright 2018 Springer Nature. Abbreviations: CNT, classical nucleation theory; NCNT, nonclassical nucleation theory.

including disordered clusters and partially ordered agglomerates of clusters, aggregate and undergo a size-induced phase transition. Although several experimental and modeling studies have explored nonclassical nucleation pathways, there is not yet a good quantitative NCNT model for understanding the mechanisms of these processes and evaluating the kinetics involved. To the best of the authors' knowledge, there has been only a limited attempt to apply NCNT in a quantitative description, specifically, by introducing excess free energy, as discussed in Section 3.3 (51). However, this term captures only net effects, and it is still difficult to experimentally quantify the multiple intermediate steps. Here, although PNCs and nanoparticles are different, studying the kinetics of nanoparticle OA can provide useful insights into building a model for nonclassical nucleation, because both nonclassical growth by OA and NCNT describe the aggregative behavior. For example, the kinetics model based on the Smoluchowski equation can be applied to NCNT (79) by considering the significant contributions of ion–solvent interactions within the PNCs to the cluster agglomeration and/or aggregation.

Whereas a holistic quantitative model that connects nucleation and growth would be ideal, for complicated systems that couple nucleation, growth, and phase transformation, developing such a comprehensive quantitative model is daunting. A good example is mesocrystal formation. In a recent in situ LP-TEM study, using aggregates of ferrihydrite as precursors, Zhu et al. found that oxalate can promote spindle-shaped hematite mesocrystal formation, but in the absence of oxalate, segregated hematite nanoparticles formed (140). In the study, dissolution of ferrihydrite provided the precursors for hematite nucleation. Importantly, the interfacial gradients of Fe^{3+} concentration at the oxalate-covered hematite surface induced new hematite nucleation adjacent to the primary hematite nanoparticles. Then, attractive particle interactions drove OA of nanoparticles to form the hematite mesocrystal. In this case, the convoluted processes of old precursor phase dissolution, new phase nucleation, and OA made the development of a quantitative description extremely difficult. To overcome this challenge, artificial intelligence technology, specifically machine learning (ML), can be an effective tool for determining and predicting multiple parameter optimization. ML has been successful in describing the physical and chemical thresholds for defining clusters, nanoparticles, and bulk states of silver (141) and in predicting and/or optimizing the synthetic nucleation and growth of CdSe or CdS (142). Future nucleation and growth investigations with ML hold great promise for describing the relative contributions from multiple processes and ultimately providing a quantitative description of complicated systems.

7.2. Connecting Experimental Data and Computational Simulations

MD has been extended continuously, including ab initio MD. Density functional theory (DFT), the dominant electronic structure method of ab initio MD, has become standard for describing and predicting the nucleation process (143). There have been many successful simulations for mineral nucleation, especially for the existence or formulation of PNCs for NCNT. For example, the DFT model quantified how solutions with different Mg:Ca ratios affect the nucleation barriers

of calcite and aragonite. The results demonstrate that the nucleation barrier of calcite exceeds that of aragonite in solutions with Mg:Ca ratios consistent with seawater (144). MD also proved that nanodroplets of dense liquid clusters coalesce and solidify into ACC (61). Furthermore, the MD method has shown the existence of mineral clusters made of ionic polymers in the shape of chains, branches, and rings as PNCs (60).

However, computational studies that better connect with experimental nucleation and growth results are still needed. For example, small systems (10^2–10^4 particles) are often modeled under ideal conditions. Because the interfacial description requires more restricted and reliable force fields, predicting a realistic nucleation system is more complicated (46). Besides, simulation results are specific to certain limited physical approximations in order to reduce the complexity of the potential. The results can be inflexible and provide only limited information on complex energy landscapes (145). Thus, future efforts should include the following:

1. To effectively determine energies and forces in large-scale simulations, we need more efficient potentials that can replace computationally extensive electronic structure calculations. For example, atomistic potentials describe the relationship between atomic configurations and potential energies. They use less sophisticated analytic functions of the atomic coordinates, which is helpful for fast evaluation of large-scale simulations (145).
2. ML potentials can directly use or combine a variety of functions, capturing various types of bonding, such as covalent bonding (146). Because the ML potentials are more general forms that, unlike classical MD, are not based on physical considerations, they can increase the simulation scale and achieve an accuracy rate closer to that of first-principles calculations (147).
3. To overcome the timescale limitation of MD simulation, new enhanced sampling techniques, such as metadynamics (148), can be developed and applied to study the nucleation. Enhanced sampling techniques are particularly useful because solid nucleation in solutions is a relatively slow process and can further be complicated by the presence of competing and complex polymorphs.

DISCLOSURE STATEMENT

The authors are not aware of any affiliations, memberships, funding, or financial holdings that might be perceived as affecting the objectivity of this review.

ACKNOWLEDGMENTS

We are grateful for the support received from the US National Science Foundation (CHE-1905077), the American Chemical Society's Petroleum Research Fund (62756-ND5), and the US Environmental Protection Agency (EPA; Assistance Agreement No. 84008401). The review has not been formally reviewed by the EPA. The views expressed in this document are solely those of the authors of this article and do not necessarily reflect those of the EPA. The EPA does not endorse any products or commercial services mentioned in this publication. We wish to thank the members of the Environmental NanoChemistry Group for their valuable discussions. We thank Prof. James Ballard, Mr. Albern Tan, and Prof. Sandra Matteucci for their careful reviews of the manuscript.

LITERATURE CITED

1. Kulmala M, Kontkanen J, Junninen H, Lehtipalo K, Manninen HE, et al. 2013. Direct observations of atmospheric aerosol nucleation. *Science* 339:943–46

2. Jung H, Lee B, Lengyel M, Axelbaum R, Yoo J, et al. 2018. Nanoscale in situ detection of nucleation and growth of Li electrodeposition at various current densities. *J. Mater. Chem. A* 6:4629–35
3. Li Q, Fernandez-Martinez A, Lee B, Waychunas GA, Jun Y-S. 2014. Interfacial energies for heterogeneous nucleation of calcium carbonate on mica and quartz. *Environ. Sci. Technol.* 48:5745–53
4. Butterfield CN, Soldatova AV, Lee S-W, Spiro TG, Tebo BM. 2013. Mn (II, III) oxidation and MnO_2 mineralization by an expressed bacterial multicopper oxidase. *PNAS* 110:11731–35
5. Byrne JM, Klueglein N, Pearce C, Rosso KM, Appel E, Kappler A. 2015. Redox cycling of Fe (II) and Fe (III) in magnetite by Fe-metabolizing bacteria. *Science* 347:1473–76
6. Jung H, Taillefert M, Sun J, Wang Q, Borkiewicz OJ, et al. 2020. Redox cycling driven transformation of layered manganese oxides to tunnel structures. *J. Am. Chem. Soc.* 142:2506–13
7. Nudelman F, Pieterse K, George A, Bomans PHH, Friedrich H, et al. 2010. The role of collagen in bone apatite formation in the presence of hydroxyapatite nucleation inhibitors. *Nat. Mater.* 9:1004–9
8. Addadi L, Raz S, Weiner S. 2003. Taking advantage of disorder: amorphous calcium carbonate and its roles in biomineralization. *Adv. Mater.* 15:959–70
9. Treat ND, Malik JAN, Reid O, Yu L, Shuttle CG, et al. 2013. Microstructure formation in molecular and polymer semiconductors assisted by nucleation agents. *Nat. Mater.* 12:628–33
10. Cleveland CL, Landman U, Schaaff TG, Shafigullin MN, Stephens PW, Whetten RL. 1997. Structural evolution of smaller gold nanocrystals: the truncated decahedral motif. *Phys. Rev. Lett.* 79:1873
11. Alivisatos AP. 1996. Semiconductor clusters, nanocrystals, and quantum dots. *Science* 271:933–37
12. Friedman G, Schultz D. 1994. Precipitation of vaterite (CaCO3) during oil field drilling. *Mineral. Mag.* 58:401–8
13. Moghadasi J, Jamialahmadi M, Müller-Steinhagen H, Sharif A, Izadpanah M, et al. 2002. *Formation damage in Iranian oil fields*. Paper presented at the International Symposium and Exhibition on Formation Damage Control, Lafayette, La., Feb.
14. Hochella MF, Lower SK, Maurice PA, Penn RL, Sahai N, et al. 2008. Nanominerals, mineral nanoparticles, and earth systems. *Science* 319:1631–35
15. Chen Q, Yuk JM, Hauwiller MR, Park J, Dae KS, et al. 2020. Nucleation, growth, and superlattice formation of nanocrystals observed in liquid cell transmission electron microscopy. *MRS Bull.* 45:713–26
16. Zhang TH, Liu XY. 2014. Experimental modelling of single-particle dynamic processes in crystallization by controlled colloidal assembly. *Chem. Soc. Rev.* 43:2324–47
17. Lioliou MG, Paraskeva CA, Koutsoukos PG, Payatakes AC. 2007. Heterogeneous nucleation and growth of calcium carbonate on calcite and quartz. *J. Colloid Interface Sci.* 308:421–28
18. Gasser U, Weeks ER, Schofield A, Pusey P, Weitz D. 2001. Real-space imaging of nucleation and growth in colloidal crystallization. *Science* 292:258–62
19. Barrere F, Snel MM, van Blitterswijk CA, de Groot K, Layrolle P. 2004. Nano-scale study of the nucleation and growth of calcium phosphate coating on titanium implants. *Biomaterials* 25:2901–10
20. Nielsen MH, Aloni S, De Yoreo JJ. 2014. In situ TEM imaging of $CaCO_3$ nucleation reveals coexistence of direct and indirect pathways. *Science* 345:1158–62
21. Xu Y, Tijssen KC, Bomans PH, Akiva A, Friedrich H, et al. 2018. Microscopic structure of the polymer-induced liquid precursor for calcium carbonate. *Nat. Commun.* 9:2582
22. Jun Y-S, Kendall TA, Martin ST, Friend CM, Vlassak JJ. 2005. Heteroepitaxial nucleation and oriented growth of manganese oxide islands on carbonate minerals under aqueous conditions. *Environ. Sci. Technol.* 39:1239–49
23. Zhang X, Shen Z, Liu J, Kerisit S, Bowden M, et al. 2017. Direction-specific interaction forces underlying zinc oxide crystal growth by oriented attachment. *Nat. Commun.* 8:835
24. Li T, Senesi AJ, Lee B. 2016. Small angle X-ray scattering for nanoparticle research. *Chem. Rev.* 116:11128–80
25. Hu Y, Lee B, Bell C, Jun Y-S. 2012. Environmentally abundant anions influence the nucleation, growth, Ostwald ripening, and aggregation of hydrous Fe (III) oxides. *Langmuir* 28:7737–46
26. Jun Y-S, Lee B, Waychunas GA. 2010. In situ observations of nanoparticle early development kinetics at mineral–water interfaces. *Environ. Sci. Technol.* 44:8182–89

27. Wu X, Lee B, Jun Y-S. 2020. Interfacial and activation energies of environmentally abundant heterogeneously nucleated iron (III)(hydr)oxide on quartz. *Environ. Sci. Technol.* 54:12119–29
28. Guinier A, Fournet G, Yudowitch KL. 1955. *Small-Angle Scattering of X-Rays*, transl. CB Walker. New York: John Wiley & Sons
29. Porod G, Glatter O, Kratky O. 1982. *Small Angle X-Ray Scattering*. London: Academic. 17 pp.
30. Yuk JM, Park J, Ercius P, Kim K, Hellebusch DJ, et al. 2012. High-resolution EM of colloidal nanocrystal growth using graphene liquid cells. *Science* 336:61–64
31. Nudelman F, Sommerdijk NA. 2011. Cryo-electron tomography: 3-dimensional imaging of soft matter. *Soft Matter* 7:17–24
32. De Yoreo JJ, Vekilov PG. 2003. Principles of crystal nucleation and growth. *Rev. Mineral.* 54:57–93
33. Ruiz-Agudo E, Putnis C. 2012. Direct observations of mineral fluid reactions using atomic force microscopy: the specific example of calcite. *Mineral. Mag.* 76:227–53
34. Wang L, Ruiz-Agudo E, Putnis CV, Menneken M, Putnis A. 2012. Kinetics of calcium phosphate nucleation and growth on calcite: Implications for predicting the fate of dissolved phosphate species in alkaline soils. *Environ. Sci. Technol.* 46:834–42
35. Cao Y, Li M, Cheng M, Song J, Hu Z. 2014. An in situ AFM investigation on the morphology of the (100) growth interface of ZTS crystal. *J. Cryst. Growth* 388:22–28
36. Teng HH, Dove PM, Orme CA, De Yoreo JJ. 1998. Thermodynamics of calcite growth: baseline for understanding biomineral formation. *Science* 282:724–27
37. Cammarata M, Levantino M, Schotte F, Anfinrud PA, Ewald F, et al. 2008. Tracking the structural dynamics of proteins in solution using time-resolved wide-angle X-ray scattering. *Nat. Methods* 5:881–86
38. Levine JR, Cohen J, Chung Y, Georgopoulos P. 1989. Grazing-incidence small-angle X-ray scattering: new tool for studying thin film growth. *J. Appl. Crystallogr.* 22:528–32
39. Rauscher M, Paniago R, Metzger H, Kovats Z, Domke J, et al. 1999. Grazing incidence small angle X-ray scattering from free-standing nanostructures. *J. Appl. Phys.* 86:6763–69
40. Zhu Y, Li Q, Kim D, Min Y, Lee B, Jun Y-S. 2021. Sulfate-controlled heterogeneous $CaCO_3$ nucleation and its non-linear interfacial energy evolution. *Environ. Sci. Technol.* 55(16):11455–64
41. Gibbs JW. 1874–78. On the equilibrium of heterogeneous substances. *Trans. Conn. Acad. Arts Sci.* 3:108–248, 343–524
42. Volmer M, Weber A. 1926. Germ-formation in oversaturated figures. *Z. Phys. Chem.* 119:277–301
43. Farkas L. 1927. Nucleation rates in supersaturated vapours. *Z. Phys. Chem.* 125:236–42
44. Becker R, Döring W. 1935. Kinetische behandlung der keimbildung in übersättigten dämpfen. *Ann. Phys. Leipz.* 416:719–52
45. Zeldovich YB. 1943. On the theory of new phase formation: cavitation. *Acta Physicochim. USSR* 18:1–22
46. Sosso GC, Chen J, Cox SJ, Fitzner M, Pedevilla P, et al. 2016. Crystal nucleation in liquids: open questions and future challenges in molecular dynamics simulations. *Chem. Rev.* 116:7078–116
47. Wagner P, Strey R. 1984. Measurements of homogeneous nucleation rates for *n*-nanone vapor using a two-piston expansion chamber. *J. Chem. Phys.* 80:5266–75
48. Liu X. 2000. Heterogeneous nucleation or homogeneous nucleation? *J. Chem. Phys.* 112:9949–55
49. Li Q, Jun Y-S. 2018. The apparent activation energy and pre-exponential kinetic factor for heterogeneous calcium carbonate nucleation on quartz. *Commun. Chem.* 1:56
50. Gebauer D, Völkel A, Cölfen H. 2008. Stable prenucleation calcium carbonate clusters. *Science* 322:1819–22
51. Habraken WJ, Tao J, Brylka LJ, Friedrich H, Bertinetti L, et al. 2013. Ion-association complexes unite classical and non-classical theories for the biomimetic nucleation of calcium phosphate. *Nat. Commun.* 4:1507
52. Hamm LM, Giuffre AJ, Han N, Tao J, Wang D, et al. 2014. Reconciling disparate views of template-directed nucleation through measurement of calcite nucleation kinetics and binding energies. *PNAS* 111:1304–9
53. Joswiak MN, Peters B, Doherty MF. 2018. Nonequilibrium kink density from one-dimensional nucleation for step velocity predictions. *Cryst. Growth Des.* 18:723–27

54. Wallace AF, DeYoreo JJ, Dove PM. 2009. Kinetics of silica nucleation on carboxyl- and amine-terminated surfaces: insights for biomineralization. *J. Am. Chem. Soc.* 131:5244–50
55. Yau S-T, Vekilov PG. 2000. Quasi-planar nucleus structure in apoferritin crystallization. *Nature* 406:494–97
56. Karthika S, Radhakrishnan T, Kalaichelvi P. 2016. A review of classical and nonclassical nucleation theories. *Cryst. Growth Des.* 16:6663–81
57. Smeets PJ, Finney AR, Habraken WJ, Nudelman F, Friedrich H, et al. 2017. A classical view on nonclassical nucleation. *PNAS* 114:E7882–90
58. Pouget EM, Bomans PH, Goos JA, Frederik PM, Sommerdijk NA. 2009. The initial stages of template-controlled $CaCO_3$ formation revealed by cryo-TEM. *Science* 323:1455–58
59. Wolf SE, Müller L, Barrea R, Kampf CJ, Leiterer J, et al. 2011. Carbonate-coordinated metal complexes precede the formation of liquid amorphous mineral emulsions of divalent metal carbonates. *Nanoscale* 3:1158–65
60. Demichelis R, Raiteri P, Gale JD, Quigley D, Gebauer D. 2011. Stable prenucleation mineral clusters are liquid-like ionic polymers. *Nat. Commun.* 2:590
61. Wallace AF, Hedges LO, Fernandez-Martinez A, Raiteri P, Gale JD, et al. 2013. Microscopic evidence for liquid-liquid separation in supersaturated $CaCO_3$ solutions. *Science* 341:885–89
62. Mancardi G, Terranova U, de Leeuw NH. 2016. Calcium phosphate prenucleation complexes in water by means of ab initio molecular dynamics simulations. *Cryst. Growth Des.* 16:3353–58
63. Yang X, Wang M, Yang Y, Cui B, Xu Z, Yang X. 2019. Physical origin underlying the prenucleation-cluster-mediated nonclassical nucleation pathways for calcium phosphate. *Phys. Chem. Chem. Phys.* 21:14530–40
64. Hu Q, Nielsen MH, Freeman C, Hamm L, Tao J, et al. 2012. The thermodynamics of calcite nucleation at organic interfaces: classical versus non-classical pathways. *Faraday Discuss.* 159:509–23
65. Burton W-K, Cabrera N, Frank F. 1951. The growth of crystals and the equilibrium structure of their surfaces. *Philos. Trans. R. Soc. A* 243:299–358
66. Chernov AA. 2012. *Modern Crystallography III: Crystal Growth*. Berlin: Springer Sci. Bus. Media
67. Choudhary MK, Jain R, Rimer JD. 2020. In situ imaging of two-dimensional surface growth reveals the prevalence and role of defects in zeolite crystallization. *PNAS* 117:28632–39
68. De Yoreo J, Zepeda-Ruiz L, Friddle R, Qiu S, Wasylenki L, et al. 2009. Rethinking classical crystal growth models through molecular scale insights: consequences of kink-limited kinetics. *Cryst. Growth Des.* 9:5135–44
69. Zhu C, Liang S, Song E, Zhou Y, Wang W, et al. 2018. In-situ liquid cell transmission electron microscopy investigation on oriented attachment of gold nanoparticles. *Nat. Commun.* 9:421
70. Van Driessche AE, Kellermeier M, Benning LG, Gebauer D. 2016. *New Perspectives on Mineral Nucleation and Growth: From Solution Precursors to Solid Materials*. Cham, Switz.: Springer
71. Zhang J, Nancollas GH. 1990. Kink densities along a crystal surface step at low temperatures and under nonequilibrium conditions. *J. Cryst. Growth* 106:181–90
72. Stack AG, Grantham MC. 2010. Growth rate of calcite steps as a function of aqueous calcium-to-carbonate ratio: independent attachment and detachment of calcium and carbonate ions. *Cryst. Growth Des.* 10:1409–13
73. Andersson M, Dobberschütz S, Sand KK, Tobler D, De Yoreo JJ, Stipp S. 2016. A microkinetic model of calcite step growth. *Angew. Chem.* 128:11252–56
74. Penn RL, Banfield JF. 1999. Morphology development and crystal growth in nanocrystalline aggregates under hydrothermal conditions: insights from titania. *Geochim. Cosmochim. Acta* 63:1549–57
75. Penn RL, Banfield JF. 1998. Imperfect oriented attachment: dislocation generation in defect-free nanocrystals. *Science* 281:969–71
76. Dirksen J, Benjelloun S, Ring T. 1990. Modelling the precipitation of copper oxalate aggregates. *Colloid Polym. Sci.* 268:864–76
77. Park J, Privman V, Matijević E. 2001. Model of formation of monodispersed colloids. *J. Phys. Chem. B* 105:11630–35
78. Huang F, Zhang H, Banfield JF. 2003. The role of oriented attachment crystal growth in hydrothermal coarsening of nanocrystalline ZnS. *J. Phys. Chem. B* 107:10470–75

79. Zhang J, Lin Z, Lan Y, Ren G, Chen D, et al. 2006. A multistep oriented attachment kinetics: coarsening of ZnS nanoparticle in concentrated NaOH. *J. Am. Chem. Soc.* 128:12981–87
80. Davis TM, Drews TO, Ramanan H, He C, Dong J, et al. 2006. Mechanistic principles of nanoparticle evolution to zeolite crystals. *Nat. Mater.* 5:400–8
81. Woehl TJ, Prozorov T. 2015. The mechanisms for nanoparticle surface diffusion and chain self-assembly determined from real-time nanoscale kinetics in liquid. *J. Phys. Chem. C* 119:21261–69
82. Hopkins JC, Podgornik R, Ching W-Y, French RH, Parsegian VA. 2015. Disentangling the effects of shape and dielectric response in van der Waals interactions between anisotropic bodies. *J. Phys. Chem. C* 119:19083–94
83. Li D, Chun J, Xiao D, Zhou W, Cai H, et al. 2017. Trends in mica–mica adhesion reflect the influence of molecular details on long-range dispersion forces underlying aggregation and coalignment. *PNAS* 114:7537–42
84. Liu L, Nakouzi E, Sushko ML, Schenter GK, Mundy CJ, et al. 2020. Connecting energetics to dynamics in particle growth by oriented attachment using real-time observations. *Nat. Commun.* 11:1045
85. De Yoreo JJ, Gilbert PU, Sommerdijk NA, Penn RL, Whitelam S, et al. 2015. Crystallization by particle attachment in synthetic, biogenic, and geologic environments. *Science* 349(6247):aaa6760
86. Liu Z, Zhang Z, Wang Z, Jin B, Li D, et al. 2020. Shape-preserving amorphous-to-crystalline transformation of $CaCO_3$ revealed by in situ TEM. *PNAS* 117:3397–404
87. Hoeher AJ, Mergelsberg ST, Borkiewicz OJ, Michel FM. 2021. Impacts of initial Ca/P on amorphous calcium phosphate. *Cryst. Growth Des.* 21(7):3736–45
88. Davis KJ, Dove PM, De Yoreo JJ. 2000. The role of Mg^{2+} as an impurity in calcite growth. *Science* 290:1134–37
89. Radha A, Fernandez-Martinez A, Hu Y, Jun Y-S, Waychunas GA, Navrotsky A. 2012. Energetic and structural studies of amorphous $Ca_{1-x}Mg_xCO_3{\cdot}nH_2O$ ($0 \leqslant x \leqslant 1$). *Geochim. Cosmochim. Acta* 90:83–95
90. Zou Z, Habraken WJ, Matveeva G, Jensen AC, Bertinetti L, et al. 2019. A hydrated crystalline calcium carbonate phase: calcium carbonate hemihydrate. *Science* 363:396–400
91. Zhu Q, Pan Z, Zhao Z, Cao G, Luo L, et al. 2021. Defect-driven selective metal oxidation at atomic scale. *Nat. Commun.* 12:558
92. Burrows ND, Hale CR, Penn RL. 2012. Effect of ionic strength on the kinetics of crystal growth by oriented aggregation. *Cryst. Growth Des.* 12:4787–97
93. Liao H-G, Zherebetskyy D, Xin H, Czarnik C, Ercius P, et al. 2014. Facet development during platinum nanocube growth. *Science* 345:916–19
94. Hu Y, Neil C, Lee B, Jun Y-S. 2013. Control of heterogeneous Fe (III)(hydr)oxide nucleation and growth by interfacial energies and local saturations. *Environ. Sci. Technol.* 47:9198–206
95. Dewan S, Carnevale V, Bankura A, Eftekhari-Bafrooei A, Fiorin G, et al. 2014. Structure of water at charged interfaces: a molecular dynamics study. *Langmuir* 30:8056–65
96. Stack AG, Raiteri P, Gale JD. 2012. Accurate rates of the complex mechanisms for growth and dissolution of minerals using a combination of rare-event theories. *J. Am. Chem. Soc.* 134:11–14
97. Kim D, Lee B, Thomopoulos S, Jun Y-S. 2018. The role of confined collagen geometry in decreasing nucleation energy barriers to intrafibrillar mineralization. *Nat. Commun.* 9:962
98. Xiao J, Qi L. 2011. Surfactant-assisted, shape-controlled synthesis of gold nanocrystals. *Nanoscale* 3:1383–96
99. Jun Y-W, Casula MF, Sim J-H, Kim SY, Cheon J, Alivisatos AP. 2003. Surfactant-assisted elimination of a high energy facet as a means of controlling the shapes of TiO_2 nanocrystals. *J. Am. Chem. Soc.* 125:15981–85
100. Werner F, Mueller CW, Thieme J, Gianoncelli A, Rivard C, et al. 2017. Micro-scale heterogeneity of soil phosphorus depends on soil substrate and depth. *Sci. Rep.* 7:3203
101. Ray JR, Lee B, Baltrusaitis J, Jun Y-S. 2012. Formation of iron (III)(hydr)oxides on polyaspartate- and alginate-coated substrates: effects of coating hydrophilicity and functional group. *Environ. Sci. Technol.* 46:13167–75
102. Liu J, Inoué S, Zhu R, He H, Hochella MF Jr. 2021. Facet-specific oxidation of Mn (II) and heterogeneous growth of manganese (oxyhydr)oxides on hematite nanoparticles. *Geochim. Cosmochim. Acta* 307:151–67

103. Elhadj S, De Yoreo JJ, Hoyer JR, Dove PM. 2006. Role of molecular charge and hydrophilicity in regulating the kinetics of crystal growth. *PNAS* 103:19237–42
104. Ohlin CA, Villa EM, Rustad JR, Casey WH. 2010. Dissolution of insulating oxide materials at the molecular scale. *Nat. Mater.* 9:11–19
105. Gonella G, Backus EHG, Nagata Y, Bonthuis DJ, Loche P, et al. 2021. Water at charged interfaces. *Nat. Rev. Chem.* 5:466–85
106. Li L, Fijneman AJ, Kaandorp JA, Aizenberg J, Noorduin WL. 2018. Directed nucleation and growth by balancing local supersaturation and substrate/nucleus lattice mismatch. *PNAS* 115:3575–80
107. Aber JE, Arnold S, Garetz BA, Myerson AS. 2005. Strong dc electric field applied to supersaturated aqueous glycine solution induces nucleation of the γ polymorph. *Phys. Rev. Lett.* 94:145503
108. Gibbs-Davis JM, Kruk JJ, Konek CT, Scheidt KA, Geiger FM. 2008. Jammed acid–base reactions at interfaces. *J. Am. Chem. Soc.* 130:15444–47
109. Katsounaros I, Meier JC, Klemm SO, Topalov AA, Biedermann PU, et al. 2011. The effective surface pH during reactions at the solid–liquid interface. *Electrochem. Commun.* 13:634–37
110. Lee SS, Koishi A, Bourg IC, Fenter P. 2021. Ion correlations drive charge overscreening and heterogeneous nucleation at solid–aqueous electrolyte interfaces. *PNAS* 118:e2105154118
111. Kendall TA, Na C, Jun YS, Martin ST. 2008. Electrical properties of mineral surfaces for increasing water sorption. *Langmuir* 24:2519–24
112. DePaolo DJ. 2011. Surface kinetic model for isotopic and trace element fractionation during precipitation of calcite from aqueous solutions. *Geochim. Cosmochim. Acta* 75:1039–56
113. Stocks-Fischer S, Galinat JK, Bang SS. 1999. Microbiological precipitation of $CaCO_3$. *Soil Biol. Biochem.* 31:1563–71
114. Schultze-Lam S, Fortin D, Davis B, Beveridge T. 1996. Mineralization of bacterial surfaces. *Chem. Geol.* 132:171–81
115. Anderson C, Pedersen K. 2003. *In situ* growth of *Gallionella* biofilms and partitioning of lanthanides and actinides between biological material and ferric oxyhydroxides. *Geobiology* 1:169–78
116. Rivadeneyra MA, Martín-Algarra A, Sánchez-Román M, Sánchez-Navas A, Martín-Ramos JD. 2010. Amorphous Ca-phosphate precursors for Ca-carbonate biominerals mediated by *Chromohalobacter marismortui*. *ISME J.* 4:922–32
117. González-Muñoz MT, Rodriguez-Navarro C, Martínez-Ruiz F, Arias JM, Merroun ML, Rodriguez-Gallego M. 2010. Bacterial biomineralization: new insights from *Myxococcus*-induced mineral precipitation. *Geol. Soc., London, Spec. Publ.* 336:31–50
118. Ferris F, Fyfe W, Beveridge T. 1987. Bacteria as nucleation sites for authigenic minerals in a metal-contaminated lake sediment. *Chem. Geol.* 63:225–32
119. Frankel RB, Bazylinski DA. 2003. Biologically induced mineralization by bacteria. *Rev. Mineral. Geochem.* 54:95–114
120. Chave KE. 1965. Carbonates: association with organic matter in surface seawater. *Science* 148:1723–24
121. Wu X, Bowers B, Kim D, Lee B, Jun Y-S. 2019. Dissolved organic matter affects arsenic mobility and iron (III)(hydr)oxide formation: implications for managed aquifer recharge. *Environ. Sci. Technol.* 53:14357–67
122. Van Driessche A, Stawski T, Kellermeier M. 2019. Calcium sulfate precipitation pathways in natural and engineered environments. *Chem. Geol.* 530:119274
123. Lau BL, Hsu-Kim H. 2008. Precipitation and growth of zinc sulfide nanoparticles in the presence of thiol-containing natural organic ligands. *Environ. Sci. Technol.* 42:7236–41
124. Barati D, Walters JD, Pajoum Shariati SR, Moeinzadeh S, Jabbari E. 2015. Effect of organic acids on calcium phosphate nucleation and osteogenic differentiation of human mesenchymal stem cells on peptide functionalized nanofibers. *Langmuir* 31:5130–40
125. Chave KE, Suess E. 1970. Calcium carbonate saturation in seawater: effects of dissolved organic matter. *Limnol. Oceanogr.* 15:633–37
126. Rose AL, Waite TD. 2002. Kinetic model for Fe(II) oxidation in seawater in the absence and presence of natural organic matter. *Environ. Sci. Technol.* 36:433–44
127. Wang Y. 2014. Nanogeochemistry: nanostructures, emergent properties and their control on geochemical reactions and mass transfers. *Chem. Geol.* 378–79:1–23

128. Yang L, Killian CE, Kunz M, Tamura N, Gilbert PUPA. 2011. Biomineral nanoparticles are space-filling. *Nanoscale* 3:603–9
129. Artusio F, Pisano R. 2018. Surface-induced crystallization of pharmaceuticals and biopharmaceuticals: a review. *Int. J. Pharm.* 547:190–208
130. Alaei A, Zong K, Asawa K, Chou T-M, Briseño AL, et al. 2021. Orienting and shaping organic semiconductor single crystals through selective nanoconfinement. *Soft Matter* 17:3603–8
131. Qian J, Gao X, Pan B. 2020. Nanoconfinement-mediated water treatment: from fundamental to application. *Environ. Sci. Technol.* 54:8509–26
132. Jiang Q, Ward MD. 2014. Crystallization under nanoscale confinement. *Chem. Soc. Rev.* 43:2066–79
133. Hamilton BD, Ha J-M, Hillmyer MA, Ward MD. 2012. Manipulating crystal growth and polymorphism by confinement in nanoscale crystallization chambers. *Acc. Chem. Res.* 45:414–23
134. Fumagalli L, Esfandiar A, Fabregas R, Hu S, Ares P, et al. 2018. Anomalously low dielectric constant of confined water. *Science* 360:1339–42
135. Le Caër S, Pin S, Esnouf S, Raffy Q, Renault JP, et al. 2011. A trapped water network in nanoporous material: the role of interfaces. *Phys. Chem. Chem. Phys.* 13:17658–66
136. Jin D, Coasne B. 2021. Reduced phase stability and faster formation/dissociation kinetics in confined methane hydrate. *PNAS* 118(16):e2024025118
137. Cantaert B, Beniash E, Meldrum FC. 2013. Nanoscale confinement controls the crystallization of calcium phosphate: relevance to bone formation. *Chem. - Eur. J.* 19:14918–24
138. Alexander B, Daulton TL, Genin GM, Lipner J, Pasteris JD, et al. 2012. The nanometre-scale physiology of bone: steric modelling and scanning transmission electron microscopy of collagen–mineral structure. *J. R. Soc. Interface* 9:1774–86
139. Kim D, Lee B, Marshall BP, Thomopoulos S, Jun Y-S. 2021. Cyclic strain enhances the early stage mineral nucleation and the modulus of demineralized bone matrix. *Biomater. Sci.* 9:5907–16
140. Zhu G, Sushko ML, Loring JS, Legg BA, Song M, et al. 2021. Self-similar mesocrystals form via interface-driven nucleation and assembly. *Nature* 590:416–22
141. Takahashi K, Takahashi L. 2019. Data driven determination in growth of silver from clusters to nanoparticles and bulk. *J. Phys. Chem. Lett.* 10:4063–68
142. Liu R, Hao J, Li J, Wang S, Liu H, et al. 2020. Causal inference machine learning leads original experimental discovery in CdSe/CdS core/shell nanoparticles. *J. Phys. Chem. Lett.* 11:7232–38
143. Marx D, Hutter J. 2009. *Ab Initio Molecular Dynamics: Basic Theory and Advanced Methods*. Cambridge, UK: Cambridge Univ. Press
144. Sun W, Jayaraman S, Chen W, Persson KA, Ceder G. 2015. Nucleation of metastable aragonite $CaCO_3$ in seawater. *PNAS* 112:3199–204
145. Behler J. 2014. Representing potential energy surfaces by high-dimensional neural network potentials. *J. Phys. Condens. Matter* 26:183001
146. Handley CM, Behler J. 2014. Next generation interatomic potentials for condensed systems. *Eur. Phys. J. B* 87:152
147. Behler J. 2016. Perspective: machine learning potentials for atomistic simulations. *J. Chem. Phys.* 145:170901
148. Gilberti F, Salvalaglio M, Parrinello M. 2015. Metadynamics studies of crystal nucleation. *IUCrJ* 2:256–66